PAPER

Towards the design of mechanically superior tubular structures for microcatheters

To cite this article: Shengwei Chen *et al* 2019 *Smart Mater. Struct.* **28** 035032

View the article online for updates and enhancements.

Recent citations

Towards the design of mechanically superior tubular structures for microcatheters

Shengwei Chen, Rohith Karthikeyan and Seok Chang Ryu[1]

Texas A & M university, Department of Mechanical Engineering, 400 Bizzell St, College Station, TX 77840, United States of America

E-mail: gottamu@tamu.edu, rohithkarthikeyan@tamu.edu and scryu@tamu.edu

Abstract

Cardiac catheterization (CC) procedures in children and adults, and especially within vasculature of small cross-section comes with the increased risk of complications due to acute occlusive arterial injuries and (or) thrombosis. Micro-catheters play a vital role in enabling CC procedures, however, to extend their functionality beyond large blood vessels and into pediatric wards, necessitates superior mechanical attributes that are fundamental to their structure. There exists a strong correlation between tool footprint and the risk of these injuries, nevertheless, changes in tool-size are impeded by mechanical constraints and manufacturing. In this paper, we propose pattern geometries for tubular structures that can be tuned to obtain desired mechanical characteristics, while retaining a minimum tool cross-section. We perform numerical simulations to systematically investigate the effect of pattern design parameters on the tube's properties, and present guidelines for obtaining the preferred behavior. The rounded re-entrant honeycomb (RRH) is introduced as the base structure for more responsive catheters, and is contrasted with the dog-bone geometry (DB), and the conventional slot. Notably, the RRH patterned tubes are highly compliant in bending yet strong in torsion while the DB tubes are strong in both torsion and bending. Therefore, our results indicate positively for a wide-range of tunable behavior in patterned tubes, with the RRH poised as a promising alternative for achieving the design goals that are introduced.

Keywords: microcatheter design, auxetics, rounded re-entrant honeycomb

(Some figures may appear in colour only in the online journal)

Nomenclature

γ	Relative torsional rigidity factor
β	Relative axial rigidity factor
η	Relative radial rigidity factor
θ	Angle between the diagonal beam and horizontal axis (degrees)
h	Length of the vertical beam in a unit cell (mm)
l	Length of the diagonal beam in a unit cell (mm)
n	Number of unit cells in the circumferential direction of the tube
r	Radius of rounded corners (mm)
r_{max}	Maximum radius of rounded corners (mm)
t	Wall thickness of the beam in a unit cell (mm)
D_o	Outer diameter of the tube (mm)
D_i	Inner diameter of the tube (mm)
L	Length of the tube (mm)
D	Diameter of fully rounded corner in the rounded re-entrant honeycomb (RRH) pattern (mm)

[1] Author to whom any corespondence should be addressed

w	Minimal gap distance in RRH pattern (mm)
D_d	Diameter of fully rounded corner in the dog-bone (DB) pattern (mm)
D_s	Diameter of fully rounded corner in the slot pattern (mm)
l_d	Distance between two ends of the DB pattern (mm)
w_d	Gap distance of the DB pattern (mm)
t_d	Distance between DB patterns in the circumferential direction (mm)
t_s	Distance between slot patterns in the circumferential direction (mm)
l_s	Length of the slot pattern (mm)
$(EI)_{eff}$	Effective flexural rigidity (N mm^2)
$(GJ)_{eff}$	Effective torsional rigidity (N mm^2)
$(E_a)_{eff}$	Effective axial rigidity (MPa)
$(E_r)_{eff}$	Effective radial rigidity (MPa)
W	Width of a unit cell (mm)
H	Height of a unit cell (mm)
ρ	Density of NiTi (kg m^{-3})
E_A	Young's modulus for austenitic NiTi (MPa)
ν_A	Poisson's ratio for austenitic NiTi
ν_{rrh}	Poisson's ratio for RRH structure
ν_{db}	Poisson's ratio for DB structure
E_M	Young's modulus for martensitic NiTi (MPa)
ν_M	Poisson's ratio for martensitic NiTi
ϵ_L	Transformation strain for NiTi
σ_L^S	Start of transformation loading (N mm^{-2})
σ_L^E	End of transformation loading (N mm^{-2})
T_0	Reference temperature (℃)
σ_U^S	Start of transformation unloading (N mm^{-2})
σ_U^E	End of transformation unloading (N mm^{-2})
σ_{CL}^S	Start of transformation loading in compression (N mm^{-2})
AS	Aspect ratio of the pattern
SS	Pattern circumference

1. Introduction

Interest in micro-catheters has surged in the past few years thanks to advancements in cardiac catheterization (CC) procedures for children as well as in small blood vessels commonly encountered in neurosurgery. CC remains a mainstay for both diagnosis and treatment of several congenital or acquired cardiac diseases in children as a way of avoiding the need for open heart surgery and the attendant long recovery times. For example, congenital atrial or ventricular-septal defects can be closed with devices that are delivered through a cardiac catheter [1] and congenital obstructed blood vessels and valves can be opened with balloon or stent technology or even replaced by trans-catheter valve placement [2]. While overall complications have been decreasing during the past years, CC in pediatric patients is still not without risk, especially since cannulation of the femoral artery is typically involved. Arterial thrombosis, or acute occlusive arterial injury (AOAI) remains one of the most reported complications of CC in children [3, 4] accounting for almost one third of all observed complications [5]. The impact may be transient or severe as it may cause skin necrosis and threaten limb viability [6]. Risk factors for AOAI have been identified [7–12] and include younger or smaller patients, use of overly large catheters, need for repeat catheterization, technique, and longer procedural time [3]. In a larger single center study, using a multi-variate model, Glatz and colleagues identified low body weight, sheath size, and a need for arterial catheter exchange as the leading risk factors [7, 12, 13]. In particular, it was found that in the smallest weight categories (<4 kg and 4–6 kg), the risk for AOAI was significantly elevated above the overall cohorts risk at 23.5% and 14.8%, respectively. The definitive correlation of overly large sheaths/catheters with increased risk of complications highlights the need for smaller equipment in pediatric patients. Furthermore, it is likely that it is the ratio of the outer diameter (OD) of the arterial catheter to the size of the cannulated artery that is the critical determinant for arterial injury risk, and arguments have been made [14] for increased risk for arterial spasm when the catheter diameter is more than 50% of the vessel luminal diameter, or when the difference between catheter and vessel diameter is less than 1.9 mm [15, 16]. This may also apply to small vessels for neurovascular catheters used for thrombus removal. The FDA has warned of potential adverse effects associated with the use of neurovascular guide catheters.

While smaller catheter sizes are known to reduce surgical complications, mechanical constraints currently limit the design of desired smaller sizes. For example, if the diameter of a regular catheter is reduced by half, its torsional rigidity is remarkably reduced as well. This significantly affects the catheters performance, since manipulation at the proximal hub may not be effectively delivered to the distal end for immediate tip response. Thus, higher torsional rigidity is critical for instant response and surgical precision. Ideally, the catheter, in addition to being smaller in diameter, would also be axially rigid for optimal stability, as well as compliant in bending. Axial rigidity, or pushability is another factor that is directly correlated with responsiveness and precision, while lower bending rigidity is essential to enable effective trackability through tortuous vessels without damage.

For isotropic and homogeneous structures, high torquability and pushability requirements are in conflict with the required bending rigidity, hindering the ideal development of such catheters. Alternatively, anisotropic structures have been proposed and fabricated based on composites (e.g. metal wire-braiding, coil-reinforcement) or on patterned anisotropic specialty metals [17]. The latter may represent the better option, as it is torsionally stronger at thinner device size, while allowing flexibility in bending. This has been leveraged
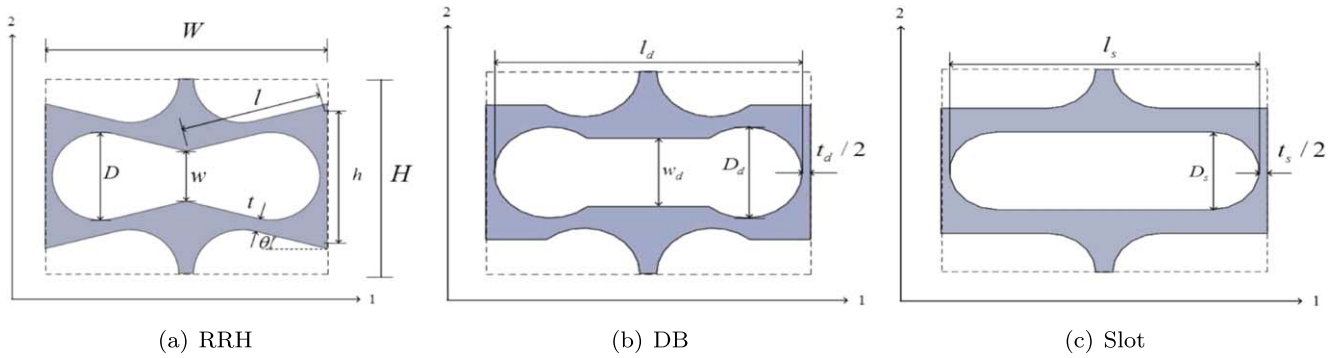
(a) RRH	(b) DB	(c) Slot

Figure 1. Geometrical shapes and parameters for the unit cells of each pattern-type. All have the same width and height.

by Boston Scientific [18], offering a commercial catheter with simple slits carved into superelastic nickel titanium (NiTi) tube for catheter diameters of around 0.7 mm. This construction can in principle, provide the desired traceability, torquability, pushability and kink-resistance, but is confined to moderate bending and twisting. This is because high curvature bending causes high stress concentrations at both ends of the slits, thus the structure becomes highly nonlinear and exhibits yield-like material behavior (i.e. it becomes weaker) which degrades torquability and decreases responsiveness of the distal tip. A more sophisticated pattern shape would be necessary to further enhance the distal tip responsiveness in tortuous vessels.

Poisson's ratio (PR), the fundamental metric governing material performance under elastic strain, differentiates auxetic and other meta-materials from common materials. More precisely, auxetic behavior is generally obtained in a class of materials that display negative PR as a result of interconnected network-like substructures that can expand laterally in size under longitudinal tension or shrink (increase density) when compressed [19]. Auxetic materials can be classified as both, structural and functional materials, allowing the overall mechanical behavior to be tailored by adjusting design parameters to meet unique performance needs, and thus, they would be one of few potential patterns for achieving a set of desired structural properties in a microcatheter. Several patents exist around the principle idea of auxetic structures for stents used during annuloplasty, angioplasty or other modes of cardiac intervention [20, 21]. Different types of negative Poisson's ratio (NPR) patterns have been developed. These include the re-entrant honeycomb (RH), chiral honeycomb [22, 23], rotating rigid structures [24–26], among other patterns [27–29]. Further, studies also investigate the suitability of RH patterns on tubular structures including [30, 31]. However, these studies are limited by the choice of constitutive behavior (linear approximation), effect of stress concentrations inherent to the pattern geometry (a limitation of non-roundedness) or a combination of these factors. The rounded re-entrant honeycomb (RRH) pattern offsets some of these issues in practice with higher rigidity in shear, lower stress concentrations due to the roundedness, and a wider range of tunable behavior, the attributes of the RRH have been studied and documented for planar cases [32, 33].

In this paper, we study an extension of the RRH pattern design toward tubular structures made from superelastic NiTi, which could potentially enable functionally augmented microcatheters. We do this by systemically investigating the effects of pattern parameters on the tube's structural properties. In addition, the effects of RRH (figure 1(a)) are compared with those of a dog-bone (DB) pattern (figure 1(b)) that was applied in the tubular structure [34] to get anisotropy, resulting in the desirable ratio (lower) of flexural rigidity to torsion rigidity [35]. The basic slot pattern (figure 1(c)) adapted in [17, 18] is also chosen as a reference pattern to investigate both the advantages and disadvantages of RRH and DB.

The design parameters of three pattern candidates and simulation models are introduced in section 2, followed by the simulation results in section 3. The effect of each design parameter on structural properties were studied, and those of RRH and DB were compared. In section 4, the large deformation behavior of patterned tubes are studied, followed by the conclusion in section 5.

2. Method

2.1. Design principles

A microcatheter's performance can be evaluated in terms of torquability, pushability, kink-resistance and trackability for precise and safe control, by measuring the relative axial rotation and displacement, radial deformation, and orientation between the distal and proximal ends. Further, we need to extend this evaluation toward applicability within small vessels encountered in pediatric and neurosurgery. The first four measures are directly related to the relative torsional, axial, radial, and bending rigidities of the device, respectively, while the last one depends on device size. Therefore, our objective in this article is to demonstrate the effect of design parameters on the rigidities of microcatheters and the extent of their tunable behavior, which would in theory enable superior devices whose axial, bending, torsional, and radial rigidities can be tailored for specific modes catheterization. This is our guiding design principle behind employing a patterned tubular structure at a clinically valid, small scale.

2.2. Design parameters

The geometric variables of RRH were: the length of the diagonal beam, l, the length of the vertical beam, h, the thickness of the thinnest part of the diagonal beam, t, and the angle between the diagonal beam and the horizontal line, θ. h/l, t/l, and θ are chosen as the dimensionless design parameters. The distance between the neighboring unit cells (dashed rectangles in figure 1) of RRH were also kept the same as t. For DB, the geometrical variables were: the diameter of the rounded end D_d, the distance between two edges of the rounded ends, l_d, and the gap width of the middle part, w_d. For slot pattern, the distance between the edges of two rounded ends, l_s, and the diameter of the rounded end, D_s were chosen as the geometrical variables. Finally, to reduce the number of variables, the dimensionless design parameters are set as h/l, t/l, and θ for RRH, and D_d/l_d, t_d/l_d, and w_d/D_d for DB.

In order to effectively compare the influence of each pattern type, the width, W, the height, H, of the unit cell for each pattern, the circumferential distance between neighbor patterns, and the diameter of ends for the three pattern-types were made identical. For this, the following relations exist:

$$l_d = l_s = W - t. \tag{1}$$

On the other hand, the diameter of the rounded end, D, and the minimal inner gap between middle, w, were selected by calculating the RRH pattern area (the white region of a unit cell in figure 1), which is,

$$S = \pi D^2 \frac{180 + 2\theta}{360} + 2(w + D\cos\theta)$$
$$\left[l\cos\theta - \frac{t}{2} - \frac{D}{2}(1 + \sin\theta) \right]) + D^2\sin\theta\cos\theta, \tag{2}$$

where D and w can be related to h and l with the following relation:

$$D = \left(h - \frac{t}{\cos\theta} - t\tan\theta \right) \tan\left(\frac{90 - \theta}{2} \right), \tag{3}$$

$$w = \left(h - \frac{t}{\cos\theta} + t\tan\theta \right) - (2l - t\cos\theta)\sin\theta. \tag{4}$$

The following geometric constraint should also be satisfied:

$$l\sin\theta < \frac{h}{2} - \frac{t}{\cos\theta} < l - \frac{t}{\cos\theta} + t\tan\theta. \tag{5}$$

The other design parameters for the RRH pattern were determined in accordance with the above equations.

Following a similar approach for the DB pattern, the pattern-area is:

$$S_d = \pi D_d^2 \frac{360 - \Gamma}{360} + w_d D_d \cos\frac{\gamma}{2} + 4l_d w_d, \tag{6}$$

where

$$\Gamma = \arccos\left(\frac{D_d^2 - 2w_d^2}{D_d^2} \right), \tag{7}$$
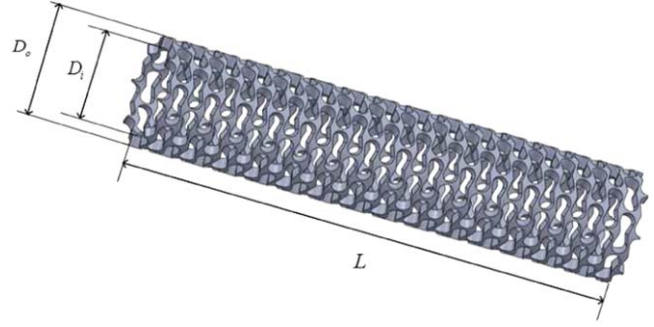

Figure 2. The shape of the patterned tube.

while the slot pattern area is

$$S_s = \pi \frac{D_s^2}{2} + 2D_s(l_s - D_s). \tag{8}$$

2.3. Tube model and metrics

The RRH patterned tube is shown in figure 2, as an example. In this study, the outer diameter of the tube was set to 1.27 mm, while the inner diameter of the tube was set to 1.0160 mm, comparable to a typical 18 Ga size medical device, while, the tube length was set to 5.74 mm, consisting of 15 rows of the model unit cell along the axial direction of the tube. The default number of unit cells along the circumferential direction of the tube was set to 8, corresponding to a sparse pattern distribution. For RRH patterns, the effects of pattern density were also evaluated by increasing the number of unit cells along the circumferential direction to 12. The material selected was NiTi, which is biocompatible and widely used in minimally invasive surgical devices. The parameters for the reference RRH model are shown in table 1.

To study the relative structural resistance between flexural deformation and the other modes of deformation, we define the relative deformation factors that follow. The relative torsional rigidity factor was defined as the ratio of effective torsional rigidity to effective flexural rigidity, which is expressed as

$$\gamma = \frac{(GJ)_{eff}}{(EI)_{eff}}. \tag{9}$$

Similarly, the relative axial rigidity factor to flexural rigidity is defined as

$$\beta = \frac{(Ea)_{eff}}{(EI)_{eff}}, \tag{10}$$

while the relative radial rigidity factor is defined as

$$\eta = \frac{(Er)_{eff}}{(EI)_{eff}}. \tag{11}$$

Table 1. Parameters of the reference RRH unit cell.

	h/l	t/l	θ	D	n	h	l	t
Sparse pattern	1	1/10	15	0.0861	8	0.2581	0.2681	0.0258
Dense pattern					12	0.1687	0.1687	0.0169

These factors were used in the current study to understand the relation between flexural deformation resistance and other deformation resistance, i.e. the torquability, pushability, and kink-resistance of a patterned tube.

For RRH, to study the effect of h/l, t/l, and θ on the structural properties described above, six models were created, with one design parameter varied with respect to the reference model. All designs had sparsely distributed patterns. The details of each model are shown in table 2.

In addition, the DB pattern unit cell was built with the same area as the RRH pattern unit cell listed in table 2, where h/l and t/l were kept the same but were represented in the form of D_d/l_d and t_d/l_d. And for the reference model, w_d/D_d was selected to be 0.5. To study the effect of D/l_d, t_d/l_d, w_d/D_d on the structural properties described above, other models were created. The set of design parameters are shown in table 3.

2.4. The simulation model

Finite element models were developed using ABAQUS commercial package [36]. The material selected for the FEM models was NiTi. In the first part of the paper, the performance of different patterned NiTi tubes in their linear ranges were explored in order to create the strategy to select better pattern candidates. In the second part of this paper, the material nonlinearity and its phase transformation were studied using the built-in NiTi model [36]. Larger deformations were applied on the NiTi tube with selected patterns. The advantages and disadvantages of each are compared according to the differing requirements. For the simulations discussed in this study, a mesh size of approximately 0.0058 mm was used, which is sufficiently small for given feature dimensions, while convergence was verified through iteration. The NiTi properties used in this study are shown in table 4, an excerpt from [37].

Four types of deformation mechanisms are studied: bending, torsional, axial, and radial. Because of the symmetry of the structure, only half of the microcatheter was selected for the simulation. The symmetric boundary condition was applied on the left surface of the tube for bending and axial deformation. For the bending simulation, the bending moment was applied on the right side of the tube. The bending curvature was measured to get the flexural rigidity. For the axial deformation simulation, the displacement was applied on the right side of the tube. The reaction force (RF) was measured to get the axial rigidity. For the torsional deformation simulation, the end of tube was fixed in the axial direction for both sides, as complimentary rotations were applied on both sides of the tube. The reaction moment (RM) on either side was measured to get the torsional rigidity. To

Table 2. Parameters of other RRH unit cell.

	h/l	t/l	θ	h	l	t
Model 1	2/3	1/10	15	0.2065	0.2582	0.0258
Model 2	5/4			0.3227	0.2582	0.0258
Model 3	1	1/20	15	0.2582	0.2582	0.0129
Model 4	1	1/5		0.2582	0.2582	0.0516
Model 5	1	1/10	5	0.2503	0.2503	0.025
Model 6			25	0.2751	0.2751	0.0275

get the radial rigidity, two additional parallel rigid plates were created and placed tangentially with respect to the tube. The plate on the bottom was fixed to support the tube while the compression displacement was applied to the upper plate. The RF on either plate was measured, and the radial rigidity was measured accordingly. For every simulation, the C3D8R element type was used.

3. Results and discussion of small-deformation performance of patterned tubes

In this section, we compare three pattern geometries on tubular structures, each having the same area of cross-section—the RRH, DB, and slot. The advantages of choosing the RRH and DB as alternatives are explored. Further, we study the effect of design parameters on both the RRH and DB patterns. In addition, we present a summary of these observations to function as design guidelines for patterned tubes with desired performance attributes.

3.1. Comparative analysis of the patterns

In catheterization procedures and other medical surgeries, flexural deformation is often the dominant mode of failure. Therefore, our first design goal is to validate the idea that the proposed pattern designs can reduce stress concentrations at the ends of the slot pattern, for tubes under bending. We performed a simulation study to validate this hypothesis.

The RRH, DB, and slot patterns were applied to tubes of a fixed length (5.74 mm). The size of each unit cell was fixed, with the RRH used as a reference geometry for each pattern type. Equations (6), (8) and the methods described in section 2.1 further outline how DB and slot patterns with the same area were created.

The three patterns were evenly distributed along the tube's circumference, and were positioned in such a way that, each tube had the same number of patterns and the same weight. For the purposes of demonstration, one end of the
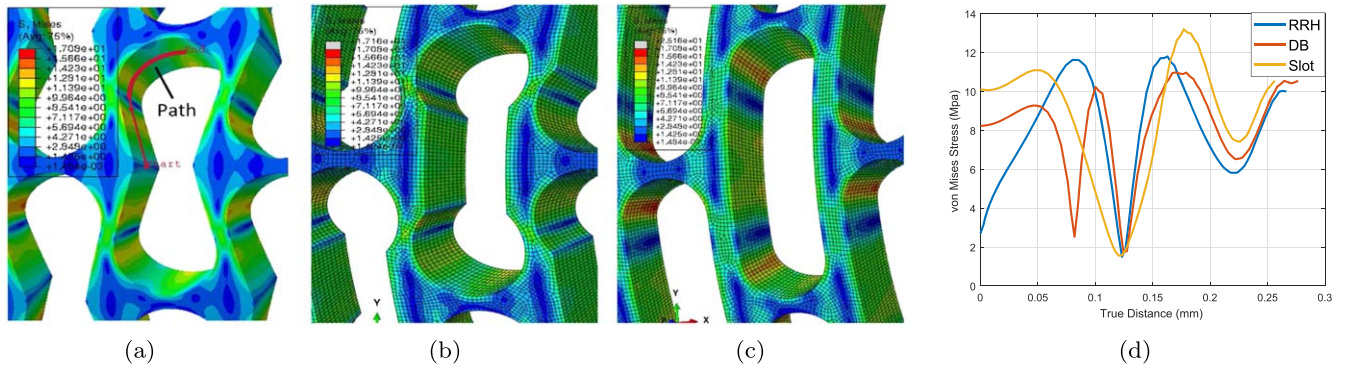
Figure 3. The stress level along the path of three different patterns: (a) RRH; (b) DB; (c) Slot; (d) the comparison of stress level of different pattern at the same location of the tube.

Table 3. Parameters of DB unit cell.

	D_d/l_d	t_d/l_d	w_d/D_d	D_d	l_d	t_d
Model 1	0.3643	0.0546	0.5	0.1723	0.4729	0.0258
Model 2	0.2247	0.0546	0.5	0.1062	0.4729	0.0258
Model 3	0.4690			0.2218	0.4729	0.0258
Model 4	0.3811	0.0256	0.5	0.1851	0.4858	0.0129
Model 5	0.3276	0.1155		0.1464	0.4471	0.0516
Model 6			0.1			
Model 7	0.3643	0.0546	0.25	0.1723	0.4729	0.0258
Model 8			0.75			

Table 4. Material properties of Nitinol.

ρ	E_A	ν_A	E_M	ν_M	ϵ_L	$(\delta\sigma/\delta T)_L$
6450 Kg m^{-3}	68000 MPa	0.3	36000 MPa	0.3	0.04	6.5

σ_L^S	σ_L^E	T_0	$(\delta\sigma/\delta T)_U$	σ_U^S	σ_U^E	σ_{CL}^S
520 MPa	635 MPa	37 °C	6.5 MPa	180 MPa	26 MPa	780 MPa

tube was fixed and a unidirectional small bending deflection (0.01 mm), was applied on the other end. To better compare and visualize the stress levels inside the geometries, three patterns were chosen at a position close to the fixed end where the observed deformation was relatively larger.

A path was created in the middle of the tube to measure the stress levels, as shown in figure 3(a). Because of the symmetry of each pattern, only a quarter of the patterns were selected to create paths. The paths started at the middle (mid-pattern) and ended in the middle of the arc segment (mid-arc).

From the results shown in figure 3(d), it is clear that peak stresses in the RRH and DB were lower than that in the slot. The peak stress level reduced by 10.59% and 16.79% in the RRH and DB pattern, respectively. Because of the flexural effect, the stress concentration was located in the immediate neighborhood of the mid-arc segment, while the stresses at the end of the three patterns was almost the same. Both peak stress levels in the RRH pattern were higher than that of the DB pattern. However, the mid-pattern structural deformations were maximal among other points within the geometry. The stress level of RRH was significantly lower than the other two, only 32.76% of DB and 26.65% of Slot. This is one of

the advantages of the hinge mechanism inside the RRH pattern, which offers more flexibility to deform and hence reduced stress levels mid-pattern. A similar hinge mechanism can be found in the DB pattern along the line that connects the flat surface to the circular segment, which explains the drop in observed stresses mid-pattern in DB geometries. Therefore, both RRH and DB could help reduce the stress concentration in the slot pattern, and can be selected as an alternative for current slot patterned tubes. The effect of design parameters for both RRH and DB are explored in the subsections to follow.

In addition, the length of the path in quarter RRH is 0.2663 mm, which is 3.72% lower than the length of DB—this can be significant. When it comes to laser fabrication, given the pattern density and count, a lower pattern-perimeter could appreciably reduce the length of the laser's path, which in-turn reduces fabrication time. Besides, the RRH has two vertices, while the DB has four, each vertex implies a change in the laser's cutting direction. Every time the laser beam changes its cutting direction, there's a pause in the movement of the laser head. However, the shutter remains open, and the beam is always focused on the workpiece. Therefore, each

Table 5. Comparison of structural properties of three patterns with the same area.

Model type	Pattern	$(EI)_{eff}$	$(GJ)_{eff}$	$(Ea)_{eff}$
Reference $\left(\frac{h}{l} = 1, \frac{t}{l} = \frac{1}{10}\right)$	RRH	43.46	63.29	791.39
	DB	56.50	67.70	858.02
	Slot	61.76	89.43	862.16
Increased t $\left(\frac{h}{l} = 1, \frac{t}{l} = \frac{1}{5}\right)$	RRH	151.16	217.19	2341.32
	DB	172.05	221.78	2322.23
	Slot	181.09	287.94	2384.36

pause can cause localized heat concentration effects along the geometry, which may affect the accuracy and also alter the material properties. Therefore, lesser the number of vertices, lesser the factors that could affect the fabricated parts. With this perspective, RRH could be more desirable than DB given practical considerations.

The properties of two sets of microcatheters with identical pattern areas were compared, as shown in table 5. It is found that for each property, RRH and DB patterned microcatheters have lower rigidities than the slot patterned one, which could help reduce the stress levels inside the pattern when the tube weights are the same. This further demonstrated that the RRH and DB could be potential alternatives to the conventional slot.

3.2. The effects of design parameters on the RRH patterned tube

The relation between each design parameter and structural properties is shown in figure 4. The relative deformation factors of the RRH are shown in table 7.

3.2.1. Effect of h/l.
The effect of h/l is shown in the figures 4(a)–(d). From the plots, when h/l increased, all $(EI)_{eff}$, $(GJ)_{eff}$, $(Ea)_{eff}$ increased, while $(Er)_{eff}$ decreased. The increment rates of $(EI)_{eff}$ and $(Ea)_{eff}$ were larger than the increment rate of $(GJ)_{eff}$. Actually, as h/l increased, the increment of GJ became less significant when compared to the increment of $(EI)_{eff}$, which is also reflected from the value of γ in table 7. γ became higher with higher h/l, which indicated that the microcatheter had a relatively higher resistance to flexural deformation when compared to torsional deformation. When h/l increased from 2/3 to 5/4, $(Ea)_{eff}$ increased the most (10.73×), followed by the increment of $(EI)_{eff}$ (10.73×), which is slightly lower than the increment of $(Ea)_{eff}$. Therefore the β values for different models were very close. The increment of $(GJ)_{eff}$ was 2.21×. Therefore, when h/l varied from 2/3 to 5/4, the tunable range of $(Ea)_{eff}$ was the highest, 1700 MPa, followed by $(EI)_{eff}$, and $(GJ)_{eff}$. $(Er)_{eff}$ decreased from 99 to 78 MPa as h/l increased. This may be caused by the decreased number of patterns in the defined distance as h/l increased. The decrease was 21.21%. When h/l became larger than 1, $(Er)_{eff}$ stopped decreasing and increased a little bit. Compared to the change

in other properties with h/l, the change in $(Er)_{eff}$ was much less significant.

3.2.2. Effect of t/l.
The effects of t/l on the structural constants are shown in figures 4(e)–(h). As t/l increased from 1/20 to 1/5, the increases in structural properties were significant, with $(EI)_{eff}$, $(GJ)_{eff}$, $(Ea)_{eff}$ and $(Er)_{eff}$ increasing by 11.62, 10.48, 8.36, and 2.91 times, respectively. Therefore, t/l had major effects on $(EI)_{eff}$ and $(GJ)_{eff}$ as these two had the largest increments. The increase of $(GJ)_{eff}$ was almost identical as the increase of $(EI)_{eff}$ with t/l, which is also reflected in the corresponding γ values. As t/l varied from 1/10 to 1/5, $(Ea)_{eff}$ had the largest tunable range, which is 2052 MPa, followed by $(GJ)_{eff}$ at 196.47 MPa, $(EI)_{eff}$ at 137 MPa, and $(Er)_{eff}$ with 89.49 MPa. The increment of $(Er)_{eff}$ was the smallest among all properties. But the effect of t/l on $(Er)_{eff}$ was discernibly greater than its effect on $(EI)_{eff}$.

3.2.3. Effect of θ.
The effects of θ on the structural constants are shown in the figures 4(i)–(l). From the results, as θ increased from 5° to 25°, the changes in $(EI)_{eff}$, $(GJ)_{eff}$, $(Ea)_{eff}$ and $(Er)_{eff}$ were negligible, which could be reflected from γ, β and η values. As θ increased from 5° to 25°, $(Ea)_{eff}$ had the largest tunable range which was 110 MPa. The tunable ranges for both $(EI)_{eff}$ and $(GJ)_{eff}$ were around 10 MPa, for $(Er)_{eff}$ it was around 30 MPa. Therefore, changing θ alone could keep the structural properties relatively stable, and provide means to make the geometrical shape compatible with the desired properties for the tube.

3.2.4. Effect of n.
The effect of n is summarized in table 6. Increasing n leads to a denser pattern distribution along the tube, increasing the structure's homogeneity. When n increased from 8 to 12, $(EI)_{eff}$, $(GJ)_{eff}$, and $(Ea)_{eff}$ increased, while $(Er)_{eff}$ decreased by a small margin. Among all of them, the change of $(EI)_{eff}$ was the largest at 18.83%. Therefore, increased n could improve the structural rigidities moderately.

The effect of design parameters of RRH could be summarized as the following:

- When h/l increased, all structural properties except $(Er)_{eff}$. The increase of $(Ea)_{eff}$ and $(EI)_{eff}$ were the highest, at 5× the increment of $(GJ)_{eff}$. The decrement of $(Er)_{eff}$ was almost negligible compared to the change in other rigidities.
- When t/l increases, all structural properties increase. The increase of $(EI)_{eff}$ and $(GJ)_{eff}$ were the highest, followed by a comparable increment of $(Ea)_{eff}$. $(Er)_{eff}$ had the smallest yet moderate increment.
- Changing θ had negligible effects on structural rigidities when compared with that of h/l and t/l.
- The increase of $(Ea)_{eff}$ was more sensitive to the increase of h/l and t/l, hence it had the largest tunable range when compared to $(EI)_{eff}$ and $(GJ)_{eff}$.
- The increment rate of $(GJ)_{eff}$ decreased at higher h/l, and increased with higher t/l. The increment rate of $(EI)_{eff}$ and $(Ea)_{eff}$ increased with both high h/l and t/l values.
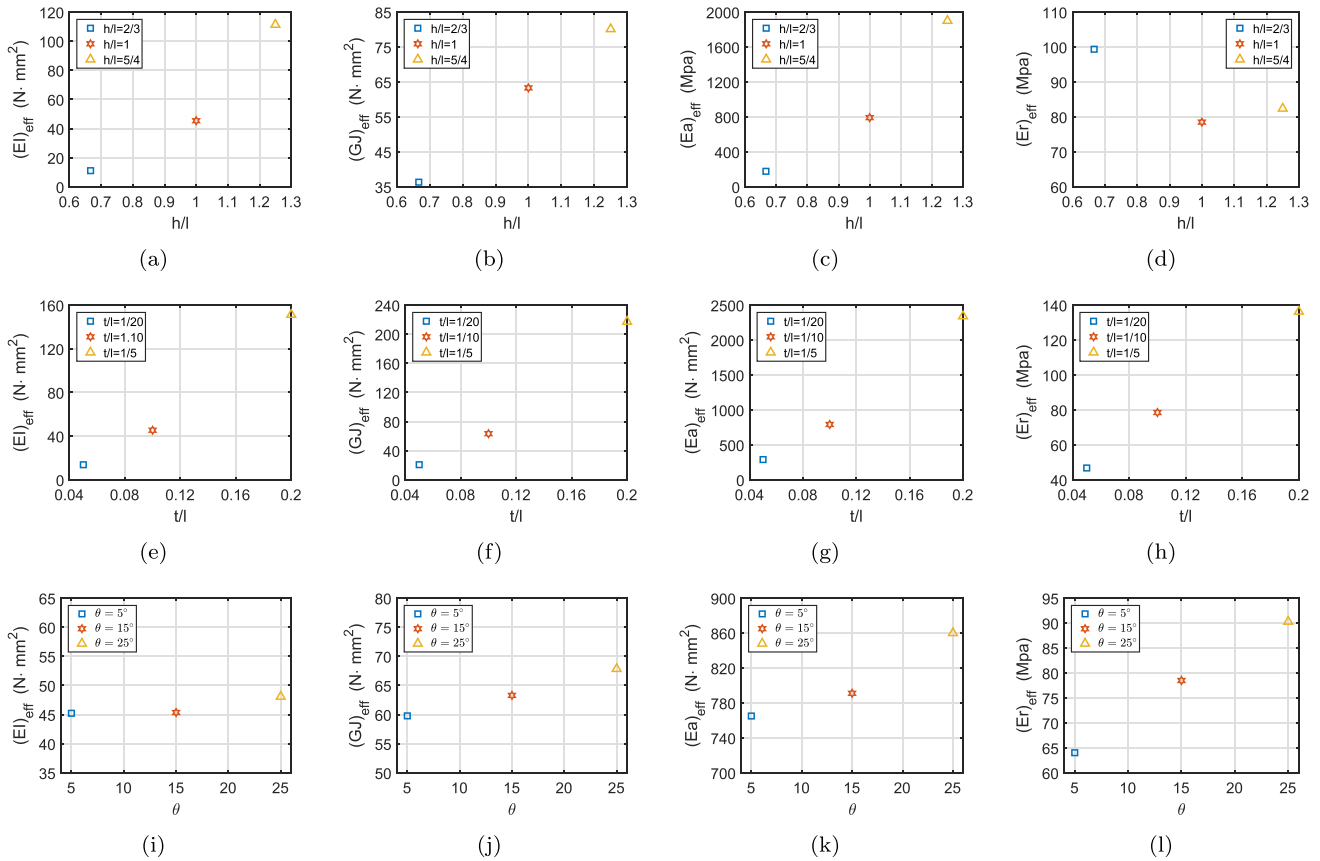
Figure 4. Structure properties versus different design parameters in the various RH cells: (a)–(d) the effect of h/l, (e)–(h) the effect of t/l, (i)–(l) the effect of θ.

Table 6. Effect of n on the structural properties.

n	$(EI)_{eff}$	$(GJ)_{eff}$	$(Ea)_{eff}$	$(Er)_{eff}$
8	45.36	63.29	791.39	78.49
12	53.09	64.57	809.49	76.44

- The structures exhibit auxetic behavior due to the NPRs (ν_{rrh}) as documented in table 7. An exception occurs at $h/l = 5/4$ which results in a value for $\gamma < 1$. Evidently, denser pattern distribution could result in further enhanced structural rigidities. The smallest feature machinable by an Nd-Yag laser for the studied size of NiTi tube is around 15 um [38], which is sufficiently small for dense pattern distributions.

3.3. The effect of design parameters on DB patterns

The relation between each design parameter and structural properties is shown in figure 5. The relative deformation factors of DB are shown in table 8.

3.3.1. Effect of D_d/l_d.
The effect of D_d/l_d was shown in figures 5(a)–(d). From the the results, as D_d/l_d increased, $(EI)_{eff}$, $(GJ)_{eff}$ and $(Ea)_{eff}$ increased as $(Er)_{eff}$ decreased. For $(EI)_{eff}$ and $(Ea)_{eff}$, the increase was at a constant rate with

Table 7. Comparison of relative deformation factors and the poisson's ratio of different RRH patterned microcatheters.

	γ	β	η	ν_{rrh}
$\frac{h}{l} = 1$	1.3954	17.4484	1.7305	-0.2834
$\frac{h}{l} = 2/3$	3.2889	16.0151	9.0002	-0.6959
$\frac{h}{l} = 5/4$	0.7197	17.0427	1.2018	0.3895
$\frac{t}{l} = 1/20$	1.5065	20.9954	3.3984	-0.3362
$\frac{t}{l} = 1/5$	1.4368	15.4889	0.9013	-0.3040
$\theta = 5°$	1.3218	16.9219	1.4157	-0.2435
$\theta = 25°$	1.4109	17.8875	1.8773	-0.2912

increase of h/l_d. However, the rate of increase of $(GJ)_{eff}$ decreased as the h/l value increased. And the rate of decrease of $(Er)_{eff}$ decreased as D_d/l_d increased. The results were very similar to the trend of RRH. As D_d/l_d increased from 0.2247 to 0.4690, $(EI)_{eff}$, $(Ea)_{eff}$, $(GJ)_{eff}$ and $(Ea)_{eff}$ increased by 16.02, 16.05 and 2.57 times, respectively, whereas $(Er)_{eff}$ decreased by 14.5%. The microcatheter became relatively rigid in torsion than in bending, as can be seen from the recorded γ_d values. This may not be an optimal choice according to our design goals.

3.3.2. Effect of t_d/l_d.
The effect of t_d/l_d is shown in figures 5(e)–(h). From the results, as t_d/l_d increased from
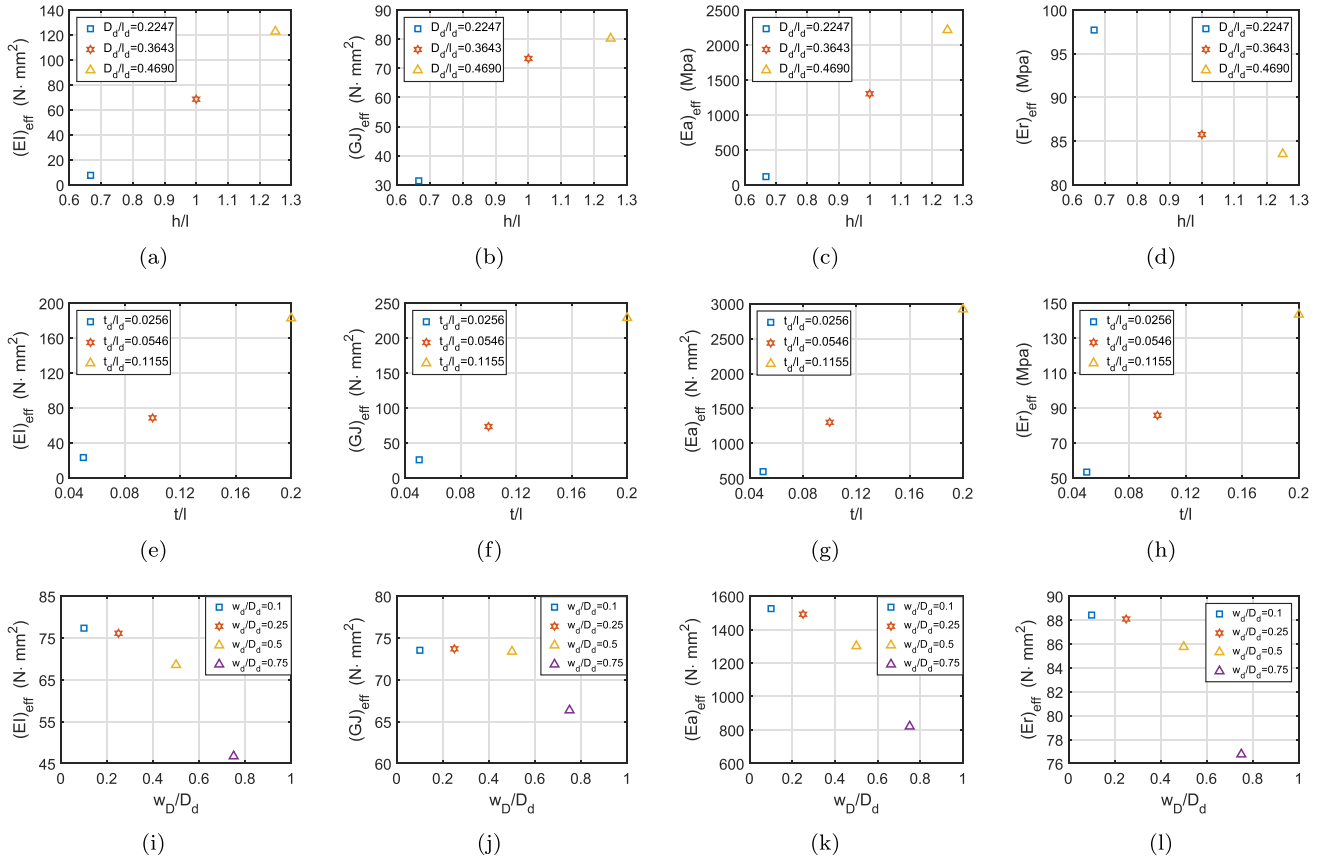
Figure 5. Structure properties versus different design parameters in the various DB cells: (a)–(d) the effect of h/l, (e)–(h) the effect of t/l, (i)–(l) the effect of w_D/D_d.

Table 8. Comparison of relative deformation factors from different DB patterned microcatheters.

	γ_d	β_d	η_d	ν_{db}
$\frac{h}{l} = 1$	1.0702	18.9863	1.2509	−0.0656
$\frac{h}{l} = 2/3$	4.1524	15.3210	12.9430	−0.7592
$\frac{h}{l} = 5/4$	0.6533	18.0276	0.6801	0.5307
$\frac{t}{l} = 1/20$	1.1097	20.7063	2.2976	−0.0989
$\frac{t}{l} = 1/5$	1.2535	15.9844	0.7856	−0.2022
$w_d/D_d = 0.1$	0.9508	19.7216	1.1432	0.0517
$w_d/D_d = 0.25$	0.9683	19.5949	1.1572	0.0327
$w_d/D_d = 0.75$	1.4203	17.5772	1.6432	−0.2959

0.0256 to 0.1155, $(EI)_{eff}$, $(GJ)_{eff}$, $(Ea)_{eff}$ and $(Er)_{eff}$ increased by 7.88, 8.90, 4.90 and 2.69 times, respectively. The increment rate was increased as t_d/l_d increased. And the microcather became relatively rigid in torsion than under felxion, as could be seen from γ_d value's increment. Even though β_d decreased by around 25%, it was still relatively strong in the axial direction, similar to the trends seen on the RRH patterns. The tunable range of Ea_{eff} was the largest, followed $(EI)_{eff}$, $(GJ)_{eff}$, and $(Ea)_{eff}$.

3.3.3. Effect of w_d/D_d.
The effect of w_d/D_d is shown in figures 5(i)–(l). As can be seen from the results, as w_D/D_d

increased, all $(EI)_{eff}$, $(GJ)_{eff}$, $(Ea)_{eff}$ and $(Er)_{eff}$ decreased. Higher the w_d/D_d, the faster the rate of decrease in structural properties. When w_d/D_d was less than 0.25, the change of structural properties was negligible. When w_d/D_d was larger than 0.5, the change became significant. When w_D/D_d equaled 1, the DB patterns were identical to the slot.

When w_d/D_d increased from 0.1 to 0.75, $(Ea)_{eff}$ decreased most (by 46.16%), followed by $(EI)_{eff}$ at 39.60%. $(GJ)_{eff}$ and $(Er)_{eff}$ had a minimal decrease at 9.74% and 13.18%, respectively. However, compared to the effect of other parameters, the change of rigidities was not so significant. But increasing w_d/D_d were practical, because the structure would be relatively rigid in torsion when compared to bending, as indicated from γ_d value.

The effect of design parameters could be summarized as the following:

- When D_d/l_d increases, all structural properties except $(Er)_{eff}$ increase. The increase of $(EI)_{eff}$ and $(Ea)_{eff}$ is much larger than the increment of $(GJ)_{eff}$. The increase of $(EI)_{eff}$ was rapid at higher D_d/l_d, while the increase of $(GJ)_{eff}$ was slower.
- When t_d/l_d increased, all structural properties increased. $(GJ)_{eff}$ increased the most, closely followed by the increase of $(EI)_{eff}$. The change in $(Er)_{eff}$ was quite moderate.
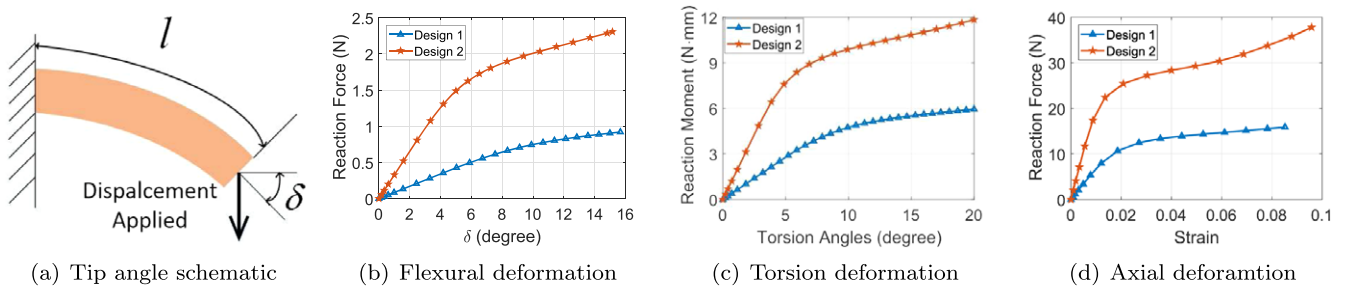
(a) Tip angle schematic   (b) Flexural deformation   (c) Torsion deformation   (d) Axial deformation

Figure 6. Comparison of two designs under larger deformation (a) bending deformation; (b) torsion deformation; (c) axial deformation.

- When w_d/D_d increased, all structural properties decreased. With a higher w_d/D_d, the structure became relatively rigid in torsion than in bending. The change of structural properties was more obvious when w_d/D_d was higher.
- The increase of $(Ea)_{eff}$ was more sensitive to the increases in D_d/l_d and t_d/l_d, hence it has the largest tunable range when compared to $(EI)_{eff}$ and $(GJ)_{eff}$.
- The increment rate of $(GJ)_{eff}$ decreased at higher D_d/l_d, and increased with higher t/l. The increment rates of $(EI)_{eff}$, $(Ea)_{eff}$ increased at both high D_d/l_d and t_d/l_d.
- The structures exhibit auxetic behavior due to the NPRs (ν_{db}) as documented in table 8. Exceptions occur at parameters which result in a value for $\gamma < 1$.

4. A design study: large-deformation performance of patterned tubes

Superelastic NiTi has a plateau region when transforming between its austenitic and martensitic phases. During this plateau-phase, the NiTi material can deform excessively even with very little increase of external force like a yielded material. Such unstable behavior can cause unexpected tissue damage that must be avoided during operation. In this section, we chose two patterned tube candidates, based on the results from previous sections, and studied their large-deformation behaviors as a fundamental component of microcatheters. The patterned tubes have relatively high torsional and axial rigidities, while low flexural rigidity (i.e. higher γ and β), which could make the tube structure behavior more predictable, safer, and responsive. Since $(Er)_{eff}$ is insensitive to the parameter changes, compared to the other rigidities, only $(EI)_{eff}$, $(GJ)_{eff}$ and $(Ea)_{eff}$ were studied.

Based on the results obtained from the previous section, there are several design approaches to achieve the design goal, including,

- Option 1 (RRH): Increase t/l and decrease h/l at the same time. To satisfy the geometrical constraint or the fabrication requirement, θ can be decrease accordingly.
- Option 2 (DB): Increase t_d/l_d, reduce D_d/l_d.
- Option 3 (DB): Increase t_d/l_d and w_d/D_d at the same time.

Table 9. Comparison of $(EI)_{eff}$ and $(GJ)_{eff}$ of two design candidates.

Geometrical change	Design 1 (RRH) increase t/l to 1/5 decrease h/l to 0.8	Design 2 (DB) increase t/l to 1/3 increase w_d/D_d to 0.8
$(EI)_{eff}$	84.02	306.69
$(GJ)_{eff}$	196.94	533.38

We chose Options 1 and 3, which are based on different patterns, RRH and DB. Also, reducing D_d/l_d in Option 2 is undesired because it could worsen either stress-concentration (by a smaller D_d) or circumferential uniformity of mechanical properties (by a longer l_d). One end of each tube was fixed (figure 6(a)), while vertical (1.2 mm, corresponding to the bending with 13.52 mm radius of curvature), rotational (20°), or axial displacement (0.5 mm) was applied on the other end. The RF—flexural and axial deformation—and RM—torsional deformation—were measured at the fixed end, while the other end deforms until the values.

Table 9 summarizes $(EI)_{eff}$ and $(GJ)_{eff}$ in the austenite phase of each Design, as well as the design approach. Both have significantly improved rigidities than the reference model. $(EI)_{eff}$ of Designs 1 and 2 correspond to that of Polyethylene catheters (75.0–94.1 MPa) and that of Nylon braided composite catheters (285–441 MPa) [39]. $(GJ)_{eff}$ of both Designs 1 and 2 interestingly corresponds to that of a larger size stainless-steel wire braided composite catheter (97 GPa). Figure 6 shows the large deformation behaviors of Designs 1 and 2, under lateral, torsional and axial deflections. It is evident that both enter the plateau region as deformation increases, resulting in nonlinear curves. The slope of the curve represents the rigidity change. As deformed, two Designs have comparable $(EI)_{eff}$ and $(GJ)_{eff}$. The $(EI)_{eff}$ at large deformation is still comparable to that of polymer catheters, while $(GJ)_{eff}$ at large deformation is still higher than that of a larger Nylon wire braided composite catheter. Also, Design 1 has smoother slope transitions, implying that more volume of material remains in the austenite phase, i.e. more uniform material phase composition. Regarding the axial rigidities, there was a little difference between the lengths of two Designs, resulting in slightly different maximum strain in figure 6(d). The linear range of RF increment for both designs was almost the same, up to about 5N (Design 1) or 10N (Design 2). Both have appropriate axial rigidities.

Based on the results, Design 1 with RRH patterns is highly compliant in bending as $(EI)_{eff}$ is comparable to monolithic polymer catheters for the wide range of deformations, while interestingly highly strong in torsion as $(GJ)_{eff}$ is comparable to or even higher than that of stainless-steel (small deflection) (97 GPa) or Nylon (large deflection) wire braided catheters (50–67 GPa). Therefore, it is not prone to sudden collapse/ kinking when compared with Design 2. On the other hand, Design 2 with DB patterns has highly strong bending and torsional rigidities, both of which are comparable to thicker stainless-steel wire braided catheters [39]. This result implies that the structural properties of a typical 18 Ga size NiTi tube can be tuned to achieve a desired set of values from the polymer to the metal wire braided composite levels. In reality, however, there are many factors that should be considered for the required performance of the microcatheter. Thus, based on the summary of the design parameters and their effects on the structure, other designs could be created to easily customize the performance of the microcatheter for the practical purpose.

5. Conclusion

In this paper, RRH and DB have been proposed as the alternative patterns which could be applied for the design of steerable microcatheters with desired mechanical properties. In this way, the catheterization procedure to treat cardiovascular disease could be safer without triggering unwanted AOAI. Compared to existing products, the stress concentration problems have been reduced. Even with smaller tube diameter employing the suggested patterns, the rigidities of the microcatheter could enhanced by manipulating design parameters. The effects of design parameters of both RRH and DB were investigated and summarized, which can be used as a guideline toward customized structural properties. In general, a microcatheter with relatively lower flexural rigidity, but with relative higher torsion, axial and radial rigidities are preferred, which is feasible by changing the design parameters as well as pattern shapes. When similar structural properties could be achieved by both RRH and DB, RRH would be more desirable because of the shorter cutting length and fewer vertices causing unwanted tube vibration, leading to more efficient fabrication speed and higher fabrication quality. The nonlinear performances of microcatheter were also explored. Different design strategies were provided to develop a desired structure according to different application requirement and preference. These properties are comparable to those of commercially available catheters.

Acknowledgments

ORCID iDs

Shengwei Chen ⬤ https://orcid.org/0000-0001-5244-9887
Rohith Karthikeyan ⬤ https://orcid.org/0000-0002-9574-6192
Seok Chang Ryu ⬤ https://orcid.org/0000-0002-6561-6880

References

[1] An Q, Zhang Z, Li J, Li F, Wu Q, Zhuang Z, Xing Q and Pan S 2010 Minimally invasive perventricular device closure of perimembranous ventricular septal defect without cardiopulmonary bypass: multicenter experience and mid-term follow-up *J. Thoracic Cardiovascular Surg.* **139** 1409–15

[2] Saliba Z, Merckx J, Aggoun Y, Bonnet D, Acar P, Le Bidois J, Sidi D, Kachaner J, Bonhoeffer P and Boudjemline Y 2000 Percutaneous replacement of pulmonary valve in a right-ventricle to pulmonary-artery prosthetic conduit with valve dysfunction *Lancet* **356** 1403–5

[3] Petry E L, Stanton R E, Lurie P R, Kirkpatrick S E and Takahashi M 1970 Percutaneous heart catheterization in infants and children. ii. Prospective study of results and complications in 127 consecutive cases *Circulation* **42** 1049–56

[4] Feliciano P, Menashe V, Sunderland C, Porter J M, Taylor L M Jr. and Troutman R 1990 Late complications after femoral artery catheterization in children less than five years of age *J. Vascular Surg.* **11** 297–306

[5] Kretschmar O, Rizzi M, Albisetti M, Brotschi B and Hug M I 2015 Incidence and predictors of cardiac catheterization-related arterial thrombosis in children *Heart* **101** 948–53

[6] de Veber G, Brookner L A, Andrew M and David M 1997 Arterial thromboembolic complications in paediatric patients *J. Thromb. Haemost.* **78** 715–25

[7] Kulkarni S and Naidu R 2006 Vascular ultrasound imaging to study immediate postcatheterization vascular complications in children *Catheterization Cardiovascular Interventions* **68** 450–5

[8] Lin P H, Dodson T F, Bush R L, Weiss V J, Conklin B S, Chen C, Chaikof E L and Lumsden A B 2001 Surgical intervention for complications caused by femoral artery catheterization in pediatric patients *J. Vascular Surg.* **34** 1071–8

[9] Hagler D J, Bailey K R, Cetta F, Phillips B L and Cabalka A K 2010 Procedural complications during congenital cardiac catheterization *Congenital Heart Dis.* **5** 118–23

[10] Saxena A, Gupta R, Kumar R K, Kothari S S and Wasir H S 1997 Predictors of arterial thrombosis after diagnostic cardiac catheterization in infants and children randomized to two heparin dosages *Catheterization Cardiovascular Interventions* **41** 400–3

[11] Vitiello R, McCrindle B W, Nykanen D, Freedom R M and Benson L N 1998 Complications associated with pediatric cardiac catheterization *J. Am. Coll. Cardiol.* **32** 1433–40

[12] Bulbul Z R, Galal M O, Mahmoud E, Narden B, Solymar L, Chaudhary M A and Al Halees Z Y 2002 Arterial complications following cardiac catheterization in children less than 10 kg *Asian Cardiovascular Thoracic Ann.* **10** 129–32

[13] Glatz A C, Shah S S, McCarthy A L, Geisser D, Daniels K, Xie D, Hanna B D, Grundmeier R W, Gillespie M J and Rome J J 2013 Prevalence of and risk factors for acute occlusive arterial injury following pediatric cardiac catheterization: a large single-center cohort study *Catheterization Cardiovascular Interventions* **82** 454–62

[14] Gold J P, Notterman D A, Steinberg C and Weinstock D J 1992 Measurements of central blood vessels in infants and children: normal values *Catheterization Cardiovascular Diagn.* **27** 197–201

[15] Franken E A Jr, Girod D, Sequeira F W, Smith W L, Hurwitz R and Smith J A 1982 Femoral artery spasm in children: catheter size is the principal cause *Am. J. Roentgenology* **138** 295–8

[16] Sahn D J, Goldberg S J, Allen H D, Valdes-Cruz L M, Canale J M, Lange L and Friedman M J 1982 A new technique for noninvasive evaluation of femoral arterial and venous anatomy before and after percutaneous cardiac catheterization in children and infants *Am. J. Cardiol.* **49** 349–55

[17] Kim J S, Baek C, Noh G, Kim D N, Kim K, Kang S, Cho K J, Lee D Y and Kim J 2015 Anisotropic patterning to reduce instability of concentric-tube robots *IEEE Transactions on Robotics* **31** 1311–23

[18] Dudeck O 2014 Safety and efficacy of target vessel catheterization with the new steerable microcatheter direxion compared with a standard microcatheter: a prospective, preclinical trial *Cardiovascular Interventional Radiol.* **37** 1041–6

[19] Anderson A 1991 A triumph of lateral thought *Chem. Ind.* **10** 384–91

[20] Burriesci G and Bergamasco G 2011 Annuloplasty prosthesis with an auxetic structure *US Patent* 8,034,103

[21] Brucker G G *et al* 2010 Bifurcated stent and delivery system *US Patent* 7,799,064

[22] Bianchi M and Scarpa F 2013 Vibration transmissibility and damping behaviour for auxetic and conventional foams under linear and nonlinear regimes *Smart Mater. Struct.* **22** 084–010

[23] Zhang D, Zhu B, Chen L, Ma Y, Scarpa F and Hong J 2013 A nonlinear auxetic structural vibration damper with metal rubber particles *Smart Mater. Struct.* **22** 084–012

[24] Kochmann D M and Venturini G N 2013 Homogenized mechanical properties of auxetic composite materials in finite-strain elasticity *Smart Mater. Struct.* **22** 084–004

[25] Dudek M R, Wojciechowski K W, Grima J N, Caruana-Gauci R and Gatt R 2013 Smart metamaterials with tunable auxetic and other properties *Smart Mater. Struct.* **22** 084–016

[26] Alderson A, Grima J N and Evans K E 2005 Auxetic behaviour from rotating rigid units *Phys. Status Solidi* b **242** 561–75

[27] Liu Y and Hu H 2010 A review on auxetic structures and polymeric materials *Adv. Mater. Sci. Eng.* **5** 1052–63

[28] Mir Mariam, Ali Murtaza Najbat, Sami Javaria and Ansari Umar 2014 Review of mechanics and applications of auxetic structures *Advances in Materials Science and Engineering* **2014** 17

[29] Evans K E and Alderson A 2000 Auxetic materials: functional materials and structures from lateral thinking *Adv. Mater.* **12** 617–28

[30] Karnessis N and Burriesci G 2013 Uniaxial and buckling mechanical response of auxetic cellular tubes *Smart Mater. Struct.* **22** 084008

[31] Ruzzene M, Scarpa F, Smith C W and Wadee M K 2008 Mechanical properties of auxetic tubular truss-like structures *Phys. Status Solidi* b **245** 584–90

[32] Chen S and Ryu S C 2017 Design and characterization of rounded re-entrant honeycomb patterns for lightweight and rigid auxetic structures *Smart Mater. Struct.* **26** 115026

[33] Harkati E H, Daoudi N E-H, Abaidia C E, Bezazi A and Scarpa F 2017 The elastic uniaxial properties of a center symmetric honeycomb with curved cell walls: effect of density and curvature *Phys. Status Solidi* b **254** 1600818

[34] Ryu S C, Renaud P, Black R J, Daniel B L and Cutkosky M R 2011 Feasibility study of an optically actuated mr-compatible active needle *Intelligent Robots and Systems (IROS), 2011 IEEE/RSJ Int. Conf. on* (IEEE) pp 2564–9

[35] Kim J-S, Lee D-Y, Kim K, Kang S and Cho K-J 2014 Toward a solution to the snapping problem in a concentric-tube continuum robot: grooved tubes with anisotropy *Robotics and Automation (ICRA), 2014 IEEE Int. Conf. on* (IEEE) pp 5871–6

[36] ABAQUS v2017. ABAQUS/Standard User's Manual. Dassault Systèmes Simulia Corp., Providence, RI, USA

[37] Azaouzi M, Makradi A and Belouettar S 2012 Deployment of a self-expanding stent inside an artery: a finite element analysis *Mater. Des.* **41** 410–20

[38] Pattanshetti S and Ryu S C 2018 Design and fabrication of laser-machined hinge joints on miniature tubes for steerable medical devices *J. Mech. Robot.* **10** 011002

[39] Munro M, Carey J and Fahim A 2004 Design of braided composite cardiovascular catheters based on required axial, flexural, and torsional rigidities *J. Biomed. Mater. Res.* B **70** 73–81